WAter Saturation Shift Referencing (WASSR) for chemical exchange saturation transfer experiments

Mina Kim[1,2], **Joseph Gillen**[1,2], **Bennett. A. Landman**[3], **Jinyuan Zhou**[1,2], and **Peter C.M. van Zijl**[1,2]

[1] Russell H. Morgan Department of Radiology and Radiological Sciences, NeuroSection, Division of MR Research, Johns Hopkins University School of Medicine, Baltimore, MD, USA

[2] F.M. Kirby Center for Functional Brain Imaging, Kennedy Krieger Institute, Baltimore, MD, USA

[3] Department of Biomedical Engineering, Johns Hopkins University School of Medicine, Baltimore, Maryland, USA

Abstract

Chemical exchange saturation transfer (CEST) is a contrast mechanism exploiting exchange-based magnetization transfer (MT) between solute and water protons. CEST effects compete with direct water saturation and conventional MT processes and generally can only be quantified through an asymmetry analysis of the water saturation spectrum (Z-spectrum) with respect to the water frequency, a process that is exquisitely sensitive to magnetic field inhomogeneities. Here, it is shown that direct water saturation imaging allows measurement of the absolute water frequency in each voxel, allowing proper centering of Z-spectra on a voxel-by-voxel basis independent of spatial B_0 field variations. Optimal acquisition parameters for this "water saturation shift referencing" or "WASSR" approach were estimated using Monte Carlo simulations and later confirmed experimentally. The optimal ratio of the WASSR sweep width to the linewidth of the direct saturation curve was found to be 3.3–4.0, requiring a sampling of 16–32 points. The frequency error was smaller than 1 Hz at signal to noise ratios of 40 or higher. The WASSR method was applied to study glycogen, where the chemical shift difference between the hydroxyl (OH) protons and bulk water protons at 3T is so small (0.75–1.25 ppm) that the CEST spectrum is inconclusive without proper referencing.

Keywords

CEST; absolute water frequency referencing; direct water saturation; glycogen; muscle

INTRODUCTION

Chemical exchange saturation transfer (CEST) has recently emerged as an alternative contrast mechanism for MRI (1–9). In this approach, selective radiofrequency (RF) irradiation of exchangeable solute protons, such as amide (NH) and hydroxyl (OH), groups (10–13), is detected through progressive saturation of the water signal consequential to chemical exchange. Chemical exchange is a well-known magnetization transfer (MT) mechanism with a single transfer pathway. As such CEST should be distinguished from conventional magnetization transfer contrast (MTC) imaging based on semi-solid protons,

Address correspondence to: Peter C.M. van Zijl, PhD, Dept. of Radiology, Johns Hopkins University School of Medicine, 217 Traylor Bldg., 720 Rutland Ave., Baltimore, MD 21205, pvanzijl@mri.jhu.edu, Tel: 443-923-9500/Fax: 443-923-9505.

where saturation transfer occurs in multiple steps, both through dipolar coupling and chemical exchange. Such indirect detection through magnetization transfer (MT) processes allows detection of species normally invisible in MRI with an effect size of a few percent on the water signal, i.e. sensitivity enhancement to the molar concentration range. For instance, CEST observation of solutes and particles in the millimolar to nanomolar range has been demonstrated both in vitro (3,6,14–17) and in vivo (10,18,19). Similar to MTC studies, CEST effects can be detected through irradiation of the proton spectrum as a function of frequency offset and measurement of the ratio of the water signal with saturation and without. A simulated example of such a water saturation spectrum, more commonly called a Z-spectrum (20) or CEST spectrum (2), is given in Fig. 1A, where a solute (amide) proton at 3.5 ppm from water shows a clear CEST effect. The large saturation effect around 0 ppm is due to direct water saturation, with the water frequency assigned to 0 ppm for reference.

CEST effects can be quite small and, if the resonance frequency of the solute protons is sufficiently close to the water frequency, the CEST effects have to compete with direct saturation (Fig. 1B). In vivo the situation is even worse, due to the occurrence of MTC effects. In order to minimize these interferences, CEST imaging generally requires an asymmetry analysis of the MT effects with respect to the water frequency, providing an MT asymmetry ratio (MTR_{asym}) spectrum. This parameter is defined as

$$MTR_{asym}(\Delta\omega) = \frac{S(-\Delta\omega) - S(\Delta\omega)}{S_0},$$

[1]

in which $\Delta\omega$ is the shift difference between the irradiation frequency and the the water center frequency and $S(\Delta\omega)$ and S_0 are the water intensities after a long presaturation pulse at the offset frequency and without a presaturation pulse, respectively. Examples of such MTR_{asym} spectra for typical examples of the NH group in proteins or the OH-group in glycogen are demonstrated by the solid curves in Figs. 1A–D. It can be seen that when the direct saturation curve is quite narrow (Figs. 1A and B), an asymmetry analysis works quite well. When the line broadens, the distinction of the CEST effect from direct saturation becomes problematic if the chemical shift difference between the solute proton and water frequency ($\Delta\omega$) is relatively small, as is the case for the hydroxyl (OH) protons of glycogen ($\Delta\omega = 0.75–1.25$ ppm, Fig. 1D). However, if the water frequency is known exactly, an asymmetry analysis still provides the correct CEST effect. Unfortunately, this seemingly simple procedure renders CEST imaging extremely sensitive to magnetic field inhomogeneities, as illustrated in Figs. 1E and F. Due to the steep slope of the direct saturation curve, even a small B_0 field difference and a concomitant shift in the Z-spectrum may cause a large change in MTR_{asym}. In vivo, where local magnetic susceptibility differences are commonplace, this effect will lead to the occurrence of artifactual signal spikes in CEST images (18,21). Depending on the solute studied, this may lead to simple errors in quantification of the magnitude of the effect, as for the amide proton in Fig. 1E, or sometimes even to total removal of the CEST effect, such as for glycogen in Fig. 1F. In addition to improving shimming, which is not likely to be sufficient in vivo, another approach to reduce this problem is to acquire images over a range of saturation frequency offsets (Z-images, typically with high saturation power), followed by polynomial or cubic-spline fitting and centering of the Z-spectrum in each voxel (10,12). This may work in vitro or even in vivo if the CEST and water saturation curves are sufficiently separated, because the direct saturation curve is symmetric and the center can be easily assigned, even if the bottom of the water saturation curve is flat and wide. However, if the CEST peak overlaps with the water resonance, as in the case for OH groups in sugars (Figs. 1D and F) (19) this approach to centering is not possible. In addition, if studies are done in vivo where the

conventional MT effect has been shown to be asymmetric (10,22,23), such an approach may be less accurate. At first glance it seems that traditional field mapping (24–28) should be able to solve this issue, but the need for at least one voxel where the exact water frequency is known prohibits application of this approach.

We here propose that absolute water frequency referencing can be accomplished by acquiring a pure direct water saturation image. This can be done by using RF irradiation that is of sufficiently small power and duration to have negligible interference of magnetization transfer effects (both MTC and CEST). To test this water saturation shift referencing (WASSR) approach, we first performed simulations to evaluate the experimental parameters needed to accurately measure the absolute water frequency in each image voxel, namely the WASSR sweep width, the saturation line width, and the number of points needed to sufficiently sample the frequency at different signal to noise ratios (SNRs). To test its feasibility, we applied WASSR to the CEST measurement of glycogen (glycoCEST, (19)), where the OH proton CEST peak cannot be visually separated from direct saturation at a field strength of 3T. This was done both in vitro and in vivo.

MATERIALS AND METHODS

Theory: WASSR with maximum–symmetry algorithm

We consider the WASSR Z-spectrum, which isolates the effect of direct water saturation. Note that the shape of the direct water saturation Z-spectrum is not affected by field inhomogeneities making it symmetric with respect to its center frequency (point of minimum intensity). Thus, the center of the direct saturation curve can be found by equalizing the frequency differences between its rising and falling slopes using a symmetry analysis. It is important to realize that the position of this symmetric line is affected by the local magnetic field, which varies between voxels due to differences in magnetic susceptibility. To determine the offset in each voxel, we used the procedure outlined in Fig. 2B. The observed signal, $f(x)$, is reflected (mirror image) with respect to the experimentally found water frequency. We then minimize the mean squared error between the measured (original) intensities and the cubic-spline interpolated intensities of the reflected curve with the following discrete energy function [2],

$$MSCF = \arg\min_{C} \left\langle \left(f(x_i) - \tilde{f}(2C - x_i) \right)^2 \right\rangle_{x_{(1)} \leq 2C - x_i \leq x_{(N)}} ,$$

[2]

in which x_i are the sampled WASSR frequency locations among N number of points ($i = 1...N$) and $\tilde{f}(2C - x_i)$ is the reflected and interpolated signal of $f(x_i)$ when C is the estimated center frequency of the original curve. The maximum-symmetry center frequency (MSCF) estimator executed argument of minimum (argmin) over a sum (< >) of mean squared error and numerical optimization was performed with Nelder-Mead simplex direct search method (29). Search initialization was achieved by selecting the median frequency of points that are at half the median intensity height. Other initializations are possible; these heuristics were chosen for convenience. Note that the mean estimated power is taken only over the points that are sampled and that, therefore, the estimate of C is restricted to the lie within the range of frequencies that are sampled. Symmetry analysis is not possible without acquiring at least some samples around the point of symmetry, which therefore requires acquisition of a minimum number of points depending on the width of the saturation curve and the chosen spectral width of the Z-spectrum. The latter depends on the range of frequency shifts over the sample.

Simulations

Monte Carlo (MC) simulations were performed to estimate the optimal parameters for WASSR imaging, including the WASSR Sweep Width (WSW) and the number of WASSR points (WN) needed to properly cover the WSW. To determine the WSW and the minimum WN, it is necessary to know the width and shape of the direct saturation curve, which was simulated using the exact steady state solution for water magnetization during saturation as provided by Mulkern and Williams (30). In terms of signal intensity, this gives:

$$S(x)/S_0 = \frac{R_1[R_2^2 + \{\Delta\omega(x)\}^2]}{R_1[R_2^2 + \{\Delta\omega(x)\}^2] + \omega_1^2 R_2},$$

[3]

in which $R_1 = 1/T_1$ (longitudinal relaxation), $R_2 = 1/T_2$ (transverse relaxation), $\omega_1 = \gamma B_1$ and $\Delta\omega = \omega - \omega_0$. $\Delta\omega$ denotes the offset of the signal point (x) with respect to the center frequency. We investigated the optimal WSW in terms of a ratio with respect to the WASSR Line Width (WLW) as defined by the Full-Width at Half Minimum of the saturation lineshape. Calculation of the line width of a lineshape such as Eq. [3] is normally done by determining the frequency offset ($\Delta\omega$) at half height ($S/S_0 = 0.5$ for full saturation). However, for the direct saturation lineshapes used here, this is not straightforward because the saturation is generally not 100% at $\Delta\omega = 0$. We therefore first calculated the actual signal intensity at $S(\Delta\omega = 0)/S_0$, subtracted this from the reference intensity ($S/S_0 = 1$) and determined the frequency at half height from that. The result is:

$$WLW(Hz) = \left(\frac{1}{\pi}\right) \sqrt{\frac{R_1 R_2^2 + \omega_1^2 R_2}{R_1}}$$

[4]

The WASSR points were applied equally spaced within the WSW as this is most practical when the field varies over a sample and shifts the saturation curve over multiple frequencies. In WASSR, the center frequency of the saturation curve needs to be found using the *maximum-symmetry algorithm* described above. We simulated the absolute error in this frequency (offset error) for different ratios WSW/WLW as a function of WN and SNR. The noise used was Rician and SNR was taken for water signal without saturation, defined as $SNR(S_0)$. To estimate the frequency shift, we modeled the center frequencies as a zero-mean normal distribution (N) with standard deviation of WLW at each spectrum as follows:

$$P(\omega_0) = N(0, WLW)$$

[5]

For each WSW/WLW ratio and WN, the expected mean absolute error was estimated with 1275 MC iterations at a simulated $SNR(S_0)$ of 100:1. The set of pairs of best WSW/WLW ratios (i.e. minimum offset error) at a certain WN was fitted with a logarithmic form to generate an expression for the optimal ratio when using a certain number of points:

$$WSW/WLW = A \times \log[WN] + B,$$

[6a]

where A and B are the fitting parameters. Using this expression, the expected WASSR offset error was computed as a function of WN for $SNR(S_0)$ values of 10:1, 20:1, 40:1, 80:1, 100:1, and 1000:1. Again, each expected WASSR error computation employed 1275 MC iterations. To determine the variability of parameter fit, these MC experiments were repeated 25 times.

Phantom

A 200mM solution of bovine liver glycogen (Type 1X G0885-25G; Sigma, St. Louis, MO) with an average molecular mass of about 50 kD was prepared by dissolving 4.98g of glycogen in 151 ml of phosphate buffered saline (pH 7.3). The glycogen concentration is expressed in glycosyl units, with each glucosyl unit contributing 168 g/mol [(4980 mg/168 mg/mmol)/151 ml) = 0.2 M].

Human subjects

Human studies were approved by the Johns Hopkins Medicine Institutional Review Board (IRB) and the Kennedy Krieger Institute, and all subjects provided signed consent. Four healthy subjects (two females and two males, 33 ± 10 years and 68 ± 9 kg, Mean $\pm$ STD) were kept in the resting state about 0.5 to 1 hour to maintain the baseline before they were scanned to measure the glycogen CEST effect in calf muscle.

MRI Acquisition

All images were acquired using a whole-body Philips 3T Achieva scanner (Philips Medical System, Best, The Netherlands) equipped with 80 mT/m gradients. RF was transmitted using the body coil and SENSE reception (31) was employed. A series of consecutive direct saturation and CEST scans were performed using the 8-element knee coil for both the glycogen phantom and in vivo human calf muscle. To minimize leg motion, foam padding was placed between the subject's lower leg and the knee coil. In all cases, second order shims over the entire muscle on the imaging slice were optimized to minimize B_0 field inhomogeneity. Notice that the width of Z-spectra depends on T_2 and that the WASSR procedure provides an absolute field frequency map so that there is no need for higher order shimming for the CEST acquisition. Clinical imagers generally employ a prescan to center the bulk water signal of the object/subject, optimize the flip angle and shim the field. Note that no such "prescan" should be made between direct saturation and CEST scans to maintain the same field reference conditions. For both scans, saturation was accomplished using a rectangular RF pulse before the turbo spin echo (TSE) image acquisition, as previously described by Jones et al. (21).

The power level needed for each saturation experiment depended on the load and was optimized by measuring sets of Z-spectra under these different conditions. For WASSR, the power and pulse lengths were chosen as small as possible to have sufficient direct saturation, while minimizing any MT effects. For CEST, the maximum pulse length allowed for the body coil within the protected clinical software (500 ms) was used and the power was optimized for maximum effect at the phantom and muscle loads. WASSR was obtained at higher frequency resolution than CEST, but over a smaller frequency range as only the direct saturation region needs to be covered. The WASSR range was chosen sufficiently large to validate the simulated results, consequently leading to a larger number of frequencies needed in vivo than for the phantom.

Single-slice glycogen phantom imaging was performed using SENSE factor = 2, TSE factor [number of refocusing pulses] = 34 (two-shots TSE), TR = 3000 ms, TE = 11 ms, matrix = 128×122, FOV = 100×100 mm^2, slice thickness = 5 mm, NSA = 1. Imaging parameters for human calf muscle experiments were identical to those in phantom experiments except for the following: FOV = 160×160 mm^2. The saturation spectral parameters for WASSR and CEST are indicated in Table 1.

Data analysis

Data were processed using a custom-written program in Matlab (Mathworks, Natick, MA, USA). For efficiency of the processing, the background around the object was masked by

excluding data points below the 50th percentile of voxel intensity. The data processing can be divided into reconstruction of a WASSR shift map and a CEST map, as shown in Fig. 2A. To create a WASSR shift map, the WASSR spectrum from each voxel was cubic-spline interpolated and the center frequency was optimized by the *maximum–symmetry algorithm* followed by search initialization of the center frequency (see details in *Theory*). The frequency difference between optimized center frequency and 0 ppm (experimental water frequency) for each voxel was stored to the WASSR shift map. To create a CEST map, the CEST spectrum in each voxel was interpolated using fast fourier transformation (FFT). First, 33 original raw CEST data points in the range of −4 to 4 ppm (frequency-domain) were transformed to the time-domain. Second, the transformed CEST data in time-domain were processed by 2 Hz line-broadening and zero-padding. Third, the processed CEST data in time-domain were inverse-transformed to frequency-domain. Overall, 33 points were interpolated to 2048 points. Subsequently, the frequency difference from the WASSR shift map was applied to correct the CEST Z-spectrum on a voxel-by-voxel basis. Finally, the MTR_{asym} intensity computed by Eq. [1] was integrated over the 0–2 ppm range on a voxel-by-voxel basis to produce the CEST map. CEST data in different regions of interest (ROIs) were quantified for 4 subjects. Four different regions of 35 ± 0.8 voxels (mean $\pm$ STD) were chosen for calf muscle in each subject.

RESULTS

Simulations

In Fig. 3A, simulations of the error in the determined center frequency of the direct saturation curve (WASSR shift map frequency) are shown as a function of the sweepwidth-to-linewidth ratio (WSW/WLW) under different sampling conditions at $SNR(S_0) = 100:1$. It can be observed that 12 WASSR points within 3.25 times WSW/LW result already in sub-Hz error. The relationship between the predicted optimal ratio (WSW/WLW at minimized mean absolute error) and number of points (BOLD line in Fig. 3A) was fitted to be:

$$WSW/WLW = (0.78 \pm 0.17) \times \log[\text{WN}] + (1.25 \pm 0.49)$$

[6b]

When plotting this optimal ratio at different WASSR resolution as a function of SNR (Fig. 3B), it is found that the estimated absolute offset error already falls into sub-Hz range when using 16 points at a $SNR(S_0)$ of 40:1 and smaller at higher SNR. Considering that the $SNR(S_0)$ for typical WASSR data is around 100:1 for humans and over 1000:1 for phantoms, these results imply that using a WSW/WLW ratio of 3.3–4 with sampling of 16–32 points is a good general guideline for WASSR imaging if the requirement for the offset error is to be less than about 0.3 Hz.

Glycogen Phantom Studies

Fig. 4A shows a typical series of CEST maps obtained for a glycogen phantom after optimized shimming, placing the transmitter offset on the average water resonance frequency, and voxel-by-voxel determination of MTR_{asym}. The CEST images are shown for the offset frequency where glycogen CEST (glycoCEST) signals are expected to be optimal (19), namely between 0.75 and 1.5 ppm from water. A clear spatial intensity fluctuation is visible even for this homogeneous solution. When looking at the corresponding CEST Z-spectrum acquired in a single voxel placed as indicated at the accompanying image, it is not clear whether the data are centered correctly, because only a single, rather broad saturation curve is visible representing the combined effects of CEST and direct saturation. However, the corresponding narrow WASSR Z-spectrum, which has negligible MTC and CEST effects due to the use of brief low power saturation, clearly shows that the spectrum was not

centered properly, resulting in a non-zero WASSR MTR_{asym}. The frequency shift of the center of the direct saturation curve in this particular voxel was only 0.08 ppm (or 10.6 Hz) off center, illustrating the exquisite sensitivity of the WASSR approach due to the steep slope of the saturation curve. Even though this shift difference is very small, the CEST MTR_{asym} spectrum (middle of Fig. 4A, solid line) shows a clear deviation from zero. The CEST maps after correction (left of Fig. 4B) show remarkable improvement in image homogeneity, compared to maps without (left of Fig. 4A). The spatial distribution of signal intensity is more uniform over the phantom and CEST maps show maximum signal in the range of about 0.75–1.25 ppm frequency offset, known to correspond to the glycogen OH proton frequency range (19). Note that the erroneous MTR_{asym} peak (right of Fig. 4A, solid line) disappears in the corrected WASSR spectrum (right of Fig. 4B, solid line), confirming that the symmetric direct saturation spectrum was centered properly.

Fig. 5 shows WASSR shift maps and CEST MTR_{asym} signal processed as a function of WN. While visual inspection of the shift maps in Fig. 5A does not show any obvious difference, the effect of WN choice on quantification is revealed clearly when looking at the actual MTR_{asym} numbers (Fig. 5B and Table 2). When using WN = 16, a glycoCEST effect that is consistent around 11.2–12.2% can be found for ROIs reflecting regions with different local fields as indicated in the accompanying reference image. The average glycoCEST effect for this phantom was 11.5%.

Human Studies

To evaluate whether the WASSR method can be used to elucidate the hidden glycoCEST effects in tissue at 3T, we performed WASSR experiment on human calf muscle. Fig. 6A shows the initial CEST maps (left) for subject S1 obtained without correction. Similar to the phantom, large signal fluctuations are found, which may be erroneously interpreted as variations in glycogen content in different muscle regions. When looking at the corresponding CEST Z-spectrum in a single voxel placed in a gastrocnemius calf muscle, it appears to be centered properly. This is due to the convolution of CEST, MTC and direct saturation effects, which, at the power level needed to see a CEST effect, merge together into a single broad saturation curve at this low field strength. However, the water offset can be easily found in the WASSR Z-spectrum, similar to the phantom results. The frequency shift of this particular voxel is about 0.08 ppm (or 10.29 Hz), while shift variation over the entire cross-section of calf muscle was found to be around 0.47 ppm (or 60 Hz) in WASSR shift maps for the four subjects (Fig. 6D). When applying the WASSR-based shift correction in each voxel, the glycoCEST maps show improved spatial homogeneity over the calf muscle (right of Fig. 6A). The corresponding CEST MTR_{asym} plot clearly shows positive signal intensity of about 6% within the expected frequency range for glycogen and close-to-zero intensity outside that range. In Fig. 6C, the integrated glycoCEST signal (range 0–2 ppm) before (left) and after (right) WASSR correction is compared for four subjects. While uncorrected glycoCEST numbers show large variations, the WASSR corrected values are more consistent and of lower standard error. The results clearly represent that glycoCEST values in different muscle regions can be quantified if proper absolute water frequency correction is applied, while uncorrected CEST values show random variation, including erroneous negative numbers.

DISCUSSION

The results show that it is possible to use direct water saturation to precisely (sub-Hz accuracy) map the absolute water frequency on a voxel-by-voxel basis. This so-called WASSR acquisition employs a brief low-power RF saturation pulse, for which magnetization transfer effects (both CEST and MTC) are expected to be negligible and for which the direct water saturation spectrum is much narrower than during the actual CEST

acquisition, where higher power broadens the curve. For this approach to be successful as reference for CEST studies, it is required to have an unchanged magnetic field between the WASSR and CEST acquisitions, which is easily feasible in practice by not performing a separate prescan (shimming and water offset determination) before the CEST acquisition that follows the WASSR mapping. As an ultimate demonstration of this approach, it was shown that glycoCEST effects could be detected at 3T in vivo in muscle even though, at this field strength, the glycoCEST resonance overlaps so much with the direct saturation curve that a separate resonance cannot be distinguished.

Technical considerations

As any other MRI approach, the accuracy of the WASSR method depends highly on the MRI parameters used to acquire the data and the experimental conditions. The parameters of interest are the line width of the direct saturation curve and the spread of the magnetic field over the region of interest, which together determine the choice of sweep width and the number of points needed to sample the frequency spread. Based on our MC simulations, the optimum range of WSW was found to be 3.3–4 times the WLW with a minimum sampling requirement of 16 points in order to achieve a sub-Hertz (< 0.3Hz) offset error for $SNR(S_0)$ values of 80 or more. The use of only a small WN is possible due to the use of a simple *maximum-symmetry* algorithm that takes into account the complete WASSR Z-spectrum to estimate the center frequency (Fig. 2B). The above sampling guideline was found to be well applicable in the glycogen phantom and in vivo in muscle, but it is possible that the WSW/WLW may have to be increased for organs with large field variations and motion effects, such as the liver. When respiratory motion is an issue, data acquisition probably will need to be triggered to the respiration to secure similar field patterns between WASSR and the CEST acquisitions. In addition, the time between the two acquisitions should be kept as short as possible. For the current study, we used comparable resolution for CEST and WASSR, but a reduction of the number of phase-encodes in WASSR by at least a factor of two should be well possible, reducing the reference scan time to only 1–2 min.

The observant reader will notice that the WASSR shift map clearly resembles a typical field map (32,33) as acquired routinely on MR scanners and may wonder whether it is possible to perform the shift centering using standard gradient-echo based field mapping. The answer is that it is not, because there is no reference voxel where the exact center frequency is known. Even though the frequency differences between all voxels are correct, the center frequency in the voxels may still be off. With respect to this, it is important to realize that, when optimizing the scanner frequency offset, the RF is placed on the water signal maximum, which is summed over the complete field of view. So there is no indication as to where the exact center is for a particular voxel within a few Hz, the precision needed for these CEST experiments. Recently Sun et al. (34) reported that B_0 field map can be used in combination with other information, such as T_1, T_2 and B_1 field maps. Although this algorithm should work for studies with small ranges of B_0 shifts, it may not be applicable for large frequency shifts that are commonplace for in vivo human data. In comparison, the algorithm described in this study requires only a WASSR map (additional scan with length of around 1–2 min), while providing reasonable correction for any shift range in B_0. An additional advantage of using a WASSR shift map instead of a field map is that WASSR and CEST experiments are obtained using identical acquisition schemes, avoiding a mismatch in field-based image distortions between the two data sets. Another suitable approach to obtain an image of absolute water frequency would be water-based spectroscopic imaging (35). This would require 2D phase encoding followed by spectral acquisition. A typical matrix of 64 × 64 at a TR of 1 s with a SENSE factor of 2 in each direction would take over 15min. As there is sufficient signal, TR can probably be reduced and a combination of such fast acquisition and time-domain analyses may be possible in the future.

Previous frequency correction approaches used cubic-spline and polynomial fitting applied to a z-spectrum acquired using the CEST acquisition parameters. WASSR, on the other hand, is an MRI acquisition method employing acquisition parameters that differ from CEST and provides an absolute water frequency map. This new principle that can be used in combination with many fitting and interpolation approaches and, as such, completely different from these previous z-spectral fitting approaches. It can be used independent of any interfering effects, such as MT asymmetry and destructive interference of CEST and direct saturation effects. One question is whether it will always be necessary to use WASSR and the answer is no. When the CEST and direct saturation effects are sufficiently separated, it may be possible to fit the exact minimum without the WASSR scans. This will be the case under conditions of sufficient SNR, spectral resolution, and sufficiently large CEST effects. However, depending on the situation studied, this may require a lengthy acquisition of the whole z-spectrum to achieve sufficient SNR or spectral resolution, which may not be feasible in vivo, especially in humans. The WASSR approach on the contrary, always provides a correct map and can be acquired rapidly (~1min), if necessary even before and after the high-SNR CEST acquisition. This will allow reduction of the number of points in the z-spectra to a few in a small frequency range around the CEST offset of interest and the mirrored reference range, so that multiple acquisitions can be done to increase SNR. Thus, WASSR is definitely necessary for glycoCEST at lower field and may be the method of choice for APT and PARACEST in cases of limited SNR and available scan time or with complex MT asymmetry patterns. Also noteworthy is that WASSR allows accuracy of a few Hz or less, i.e. a few hundredths of a ppm while rapidly acquiring only 16–32 spectral points with single acquisition.

Application to glycoCEST MRI

As a first demonstration of the WASSR method, we studied a phantom with bovine liver glycogen (200 mM) and tried to detect glycogen signals in the human calf muscle in vivo. The glycogen hydroxyl groups resonate around 0.75 and 1.25 ppm from water (19) and, at the RF power levels needed for proper CEST magnetization transfer, cannot be distinguished as a separate resonance in the Z-spectrum at the field of 3T. In the phantom, the glycoCEST effect thus appears as an asymmetric broadening of the direct water saturation curve, thereby complicating its detection (Fig. 4) due to uncertainty about the exact water frequency offset. Without the WASSR referencing the CEST maps showed positive and negative MTR asymmetries indicating that it is not possible to reproducibly discern glycogen. When correcting for the absolute water frequency using WASSR (Fig. 5), a homogeneous glycogen distribution could be detected when using 16 or more points for the frequency mapping, in line with expectations based on our simulations. The averaged MTR_{asym} for 200 mM glycogen was about $11.5 \pm 0.6\%$.

As a first in vivo application, we studied the potential of WASSR to assist in detection glycogen in the calf muscle. The results for four subjects showed that WASSR correction was essential to find reproducibly positive glycoCEST effects (Fig. 6C). This should open up the way for in vivo glycogen MRI studies, which may add diagnostic capability for many common diseases, including obesity, insulin resistance and Type-2 diabetes. The resulting quantified CEST effects in Table 3 give a range of MTR_{asym} values of 4.8–5.5% for four different muscles, the soleus, the medial and lateral heads of the gastrocnemius, and the tibialis anterior. Based on the phantom result, this would correspond to a glycogen concentration of around 100 mM or less in the leg, which is not unreasonable in view of the literature value of around 50–100 mM (36). As the CEST effect is complex and its quantification depends on many parameters, including T_1, T_2, pH, scan repetition time, and even B_1, a more detailed study comparing glycoCEST with the gold-standard 13C studies

(37,38) is needed to better assess absolute quantification. Such a study is currently being designed.

CONCLUSIONS

A new absolute water frequency mapping approach was demonstrated that employs the direct water saturation obtained with a brief low power RF pulse. Guidelines for choice of sweep-width and sampling rate were provided. As a first demonstration, this so-called WASSR approach was applied to center the Z-spectrum of glycogen in phantoms, where the OH groups resonate so close to the water protons that the CEST and direct water saturation resonances are convolved even at 3T. The resulting data show that WASSR allowed identification of glycoCEST effects in both phantoms and the human calf muscle. The WASSR correction method is expected to be beneficial for accurate quantification of CEST effects with wide range of application both in vivo tissue and in vitro with MRI and MRS.

Acknowledgments

References

1. Ward KM, Aletras AH, Balaban RS. A new class of contrast agents for MRI based on proton chemical exchange dependent saturation transfer (CEST). J Magn Reson 2000;143(1):79–87. [PubMed: 10698648]

2. Ward KM, Balaban RS. Determination of pH using water protons and chemical exchange dependent saturation transfer (CEST). Magn Reson Med 2000;44(5):799–802. [PubMed: 11064415]

3. Goffeney N, Bulte JW, Duyn J, Bryant LH Jr, van Zijl PC. Sensitive NMR detection of cationic-polymer-based gene delivery systems using saturation transfer via proton exchange. J Am Chem Soc 2001;123(35):8628–8629. [PubMed: 11525684]

4. Zhou J, van Zijl PC. Chemical exchange saturation transfer imaging and spectroscopy. Progr NMR Spectr 2006;48(2–3):109–136.

5. Zhang S, Merritt M, Woessner DE, Lenkinski RE, Sherry AD. PARACEST agents: modulating MRI contrast via water proton exchange. Acc Chem Res 2003;36(10):783–790. [PubMed: 14567712]

6. Aime S, Barge A, Delli Castelli D, Fedeli F, Mortillaro A, Nielsen FU, Terreno E. Paramagnetic lanthanide(III) complexes as pH-sensitive chemical exchange saturation transfer (CEST) contrast agents for MRI applications. Magn Reson Med 2002;47(4):639–648. [PubMed: 11948724]

7. Aime S, Delli Castelli D, Fedeli F, Terreno E. A paramagnetic MRI-CEST agent responsive to lactate concentration. J Am Chem Soc 2002;124(32):9364–9365. [PubMed: 12167018]

8. Yoo B, Pagel MD. A PARACEST MRI contrast agent to detect enzyme activity. J Am Chem Soc 2006;128(43):14032–14033. [PubMed: 17061878]

9. Liu G, Li Y, Pagel MD. Design and characterization of a new irreversible responsive PARACEST MRI contrast agent that detects nitric oxide. Magn Reson Med 2007;58(6):1249–1256. [PubMed: 18046705]

10. Zhou J, Payen JF, Wilson DA, Traystman RJ, van Zijl PC. Using the amide proton signals of intracellular proteins and peptides to detect pH effects in MRI. Nat Med 2003;9(8):1085–1090. [PubMed: 12872167]

11. van Zijl PC, Zhou J, Mori N, Payen JF, Wilson D, Mori S. Mechanism of magnetization transfer during on-resonance water saturation. A new approach to detect mobile proteins, peptides, and lipids. Magn Reson Med 2003;49(3):440–449. [PubMed: 12594746]

12. Zhou J, Lal B, Wilson DA, Laterra J, van Zijl PC. Amide proton transfer (APT) contrast for imaging of brain tumors. Magn Reson Med 2003;50(6):1120–1126. [PubMed: 14648559]

13. Ling W, Regatte RR, Navon G, Jerschow A. Assessment of glycosaminoglycan concentration in vivo by chemical exchange-dependent saturation transfer (gagCEST). Proc Natl Acad Sci U S A 2008;105(7):2266–2270. [PubMed: 18268341]

14. Snoussi K, Bulte JW, Gueron M, van Zijl PC. Sensitive CEST agents based on nucleic acid imino proton exchange: detection of poly(rU) and of a dendrimer-poly(rU) model for nucleic acid delivery and pharmacology. Magn Reson Med 2003;49(6):998–1005. [PubMed: 12768576]

15. Aime S, Delli Castelli D, Lawson D, Terreno E. Gd-loaded liposomes as T1, susceptibility, and CEST agents, all in one. J Am Chem Soc 2007;129(9):2430–2431. [PubMed: 17288421]

16. Zhang S, Winter P, Wu K, Sherry AD. A novel europium(III)-based MRI contrast agent. J Am Chem Soc 2001;123(7):1517–1518. [PubMed: 11456734]

17. Woods M, Woessner DE, Zhao P, Pasha A, Yang MY, Huang CH, Vasalitiy O, Morrow JR, Sherry AD. Europium(III) macrocyclic complexes with alcohol pendant groups as chemical exchange saturation transfer agents. J Am Chem Soc 2006;128(31):10155–10162. [PubMed: 16881645]

18. Gilad AA, McMahon MT, Walczak P, Winnard PT Jr, Raman V, van Laarhoven HW, Skoglund CM, Bulte JW, van Zijl PC. Artificial reporter gene providing MRI contrast based on proton exchange. Nat Biotechnol 2007;25(2):217–219. [PubMed: 17259977]

19. van Zijl PC, Jones CK, Ren J, Malloy CR, Sherry AD. MRI detection of glycogen in vivo by using chemical exchange saturation transfer imaging (glycoCEST). Proc Natl Acad Sci U S A 2007;104(11):4359–4364. [PubMed: 17360529]

20. Bryant RG. The dynamics of water-protein interactions. Annu Rev Biophys Biomol Struct 1996;25:29–53. [PubMed: 8800463]

21. Jones CK, Schlosser MJ, van Zijl PC, Pomper MG, Golay X, Zhou J. Amide proton transfer imaging of human brain tumors at 3T. Magn Reson Med 2006;56(3):585–592. [PubMed: 16892186]

22. Pekar J, Jezzard P, Roberts DA, Leigh JS Jr, Frank JA, McLaughlin AC. Perfusion imaging with compensation for asymmetric magnetization transfer effects. Magn Reson Med 1996;35(1):70–79. [PubMed: 8771024]

23. Swanson SD. Protein mediated magnetic coupling between lactate and water protons. J Magn Reson 1998;135(1):248–255. [PubMed: 9799702]

24. Prammer MG, Haselgrove JC, Shinnar M, Leigh JS Jr. A new approach to automatic shimming. J Magn Reson 1988;77(11):40–52.

25. Schneider E, Glover G. Rapid in vivo proton shimming. Magn Reson Med 1991;18(2):335–347. [PubMed: 2046515]

26. Webb P, Macovski A. Rapid, fully automatic, arbitrary-volume in vivo shimming. Magn Reson Med 1991;20(1):113–122. [PubMed: 1943653]

27. Maudsley AA, Simon HE, Hilal SK. Magnetic field measurement by NMR imaging. J Phys E: Sci Instrum 1984;17(3):216–220.

28. Tropp JS, Derby KA, Hawryszko C, Sugiura S, Yamagata H. Automated shimming of B0 for spectroscopic imaging. J Magn Reson 1989;85:244–254.

29. Lagarias JC, Reeds JA, Wright MH, Wright PE. Convergence Properties of the Nelder--Mead Simplex Method in Low Dimensions. SIAM J on Optimization 1998;9(1):112–147.

30. Mulkern RV, Williams ML. The general solution to the Bloch equation with constant rf and relaxation terms: application to saturation and slice selection. Med Phys 1993;20(1):5–13. [PubMed: 8455512]

31. Pruessmann KP, Weiger M, Scheidegger MB, Boesiger P. SENSE: sensitivity encoding for fast MRI. Magn Reson Med 1999;42(5):952–962. [PubMed: 10542355]

32. Webb P, Spielman D, Macovski A. Inhomogeneity correction for in vivo spectroscopy by high-resolution water referencing. Magn Reson Med 1992;23(1):1–11. [PubMed: 1734171]

33. Dagher, AP.; Balaban, RS.; Aletras, A. BEST-CEST: B0-Error Shift Tracking Chemical Exchange Saturation Transfer Imaging. Proceedings of the 10th Annual Meeting of ISMRM; Honolulu, Hawaii, USA. 2002. p. 611

34. Sun PZ, Farrar CT, Sorensen AG. Correction for artifacts induced by B(0) and B(1) field inhomogeneities in pH-sensitive chemical exchange saturation transfer (CEST) imaging. Magn Reson Med 2007;58(6):1207–1215. [PubMed: 17969015]

35. Spielman D, Webb P, Macovski A. Water referencing for spectroscopic imaging. Magn Reson Med 1989;12(1):38–49. [PubMed: 2607959]

36. Price TB, Rothman DL, Avison MJ, Buonamico P, Shulman RG. 13C-NMR measurements of muscle glycogen during low-intensity exercise. J Appl Physiol 1991;70(4):1836–1844. [PubMed: 2055862]

37. Cline GW, Petersen KF, Krssak M, Shen J, Hundal RS, Trajanoski Z, Inzucchi S, Dresner A, Rothman DL, Shulman GI. Impaired glucose transport as a cause of decreased insulin-stimulated muscle glycogen synthesis in type 2 diabetes. N Engl J Med 1999;341(4):240–246. [PubMed: 10413736]

38. Magnusson I, Rothman DL, Katz LD, Shulman RG, Shulman GI. Increased rate of gluconeogenesis in type II diabetes mellitus. A 13C nuclear magnetic resonance study. J Clin Invest 1992;90(4):1323–1327. [PubMed: 1401068]
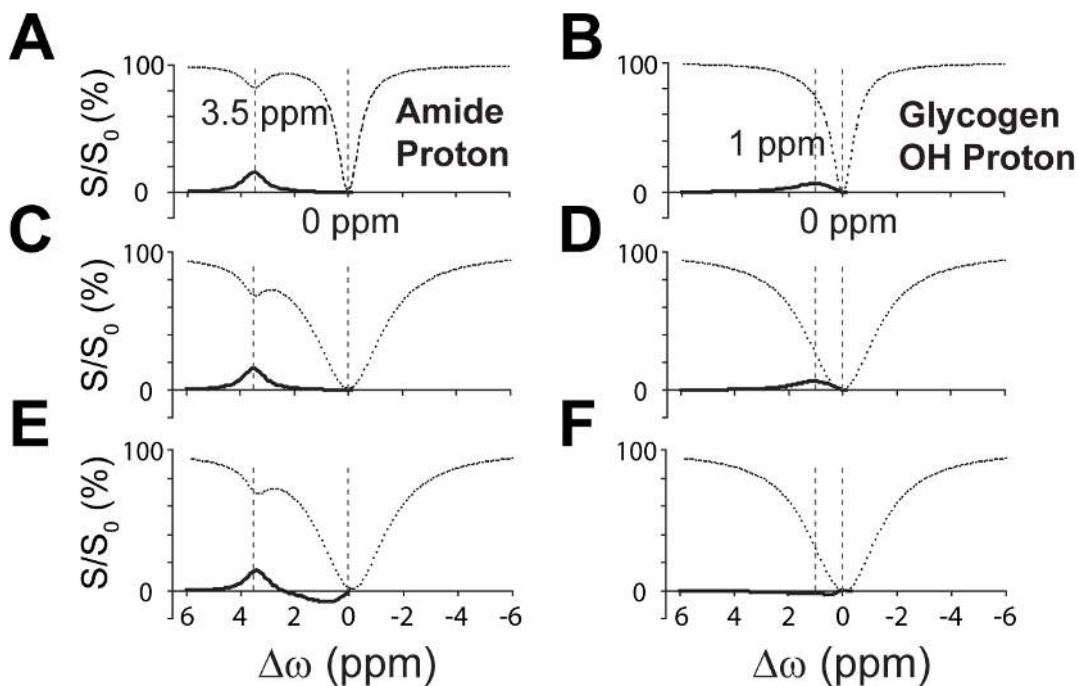
Figure 1. Simulated Z-spectra (dashed lines) and *MTR*_{asym} plots (solid lines) for an amide proton (A, C, E) and a glycogen OH proton (B, D, F)

The large intensity drop around 0 ppm is due to direct water saturation, with the water frequency assigned to 0 ppm. (A) An amide proton at 3.5 ppm shows a clear CEST effect in both Z-spectrum and MTR_{asym} plot. (B) A glycogen OH proton at 1 ppm shows relatively clear but small CEST effect in the MTR_{asym} plot, but the CEST effect is not clearly visible in the Z-spectrum because the OH protons resonate close to the water frequency. When the direct saturation lineshape broadens (C, D), the CEST effects of the amide and OH protons can be still observed in the MTR_{asym} plot as long as the saturation curve is properly centered. However, a shift as small as 0.1 ppm in the Z-spectra can cause relatively large changes in MTR_{asym}, affecting the CEST quantification of the amide proton (E) and obliviating the CEST effect of the OH proton (F).
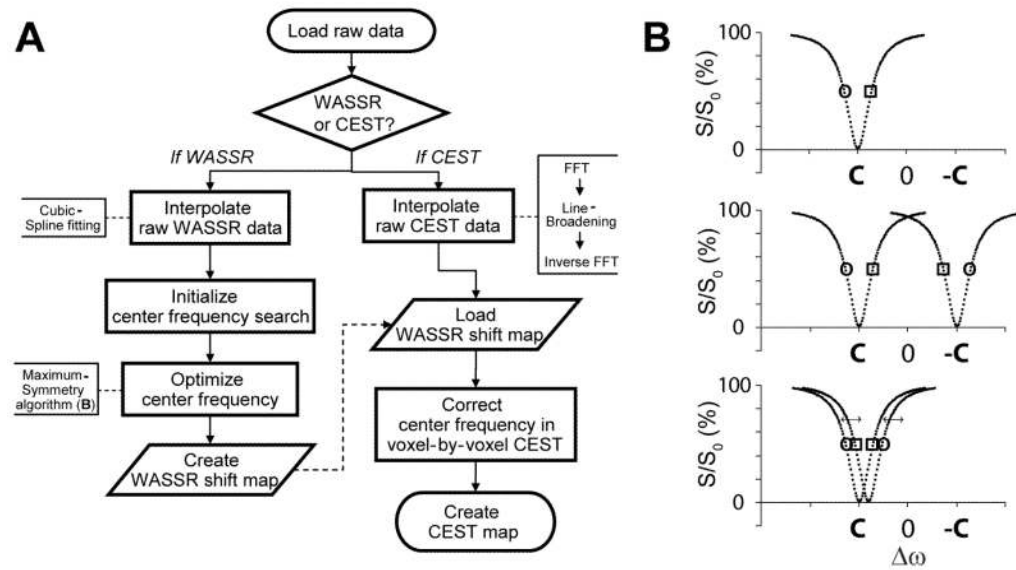
Figure 2. Data processing procedures
(A) Flow Chart. The procedures are divided into 1) generation of WASSR shift map and 2) correction of CEST data using WASSR shift map. (B) The maximum–symmetry algorithm utilized to determine the offset in each voxel. The curve is flipped around the frequency offset and then merged to determine the offset frequency *C*. For more detail, see Materials and Methods.
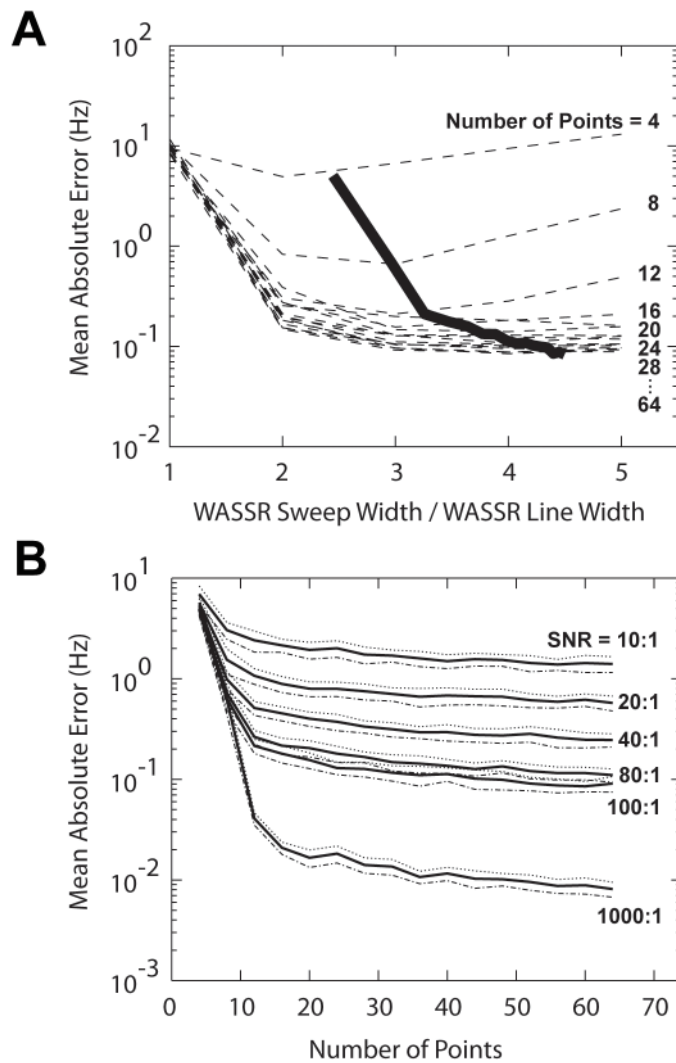
Figure 3. Simulations of offset error (logarithmic scale) in the WASSR center frequency
(A) Offset error as a function sweepwidth/linewidth (WSW/WLW) ratio for different
sampling resolutions at an SNR of 100:1 for water signal that is not saturated (S_0). The bold
line shows the predicted "optimal" WSW/WLW at each number of points and is described
as an expression of [WSW/WLW = (0.78±0.17) × log(number of points) + (1.25±0.49)]. It is
observed that twelve WASSR points within 3.25 x WSW/WLW result in sub-Hz error. (B)
Using the equation for optimal WSW/WLW at each number of points, the estimated error
curves are plotted in solid lines with respect to each number of points at various SNRs. The
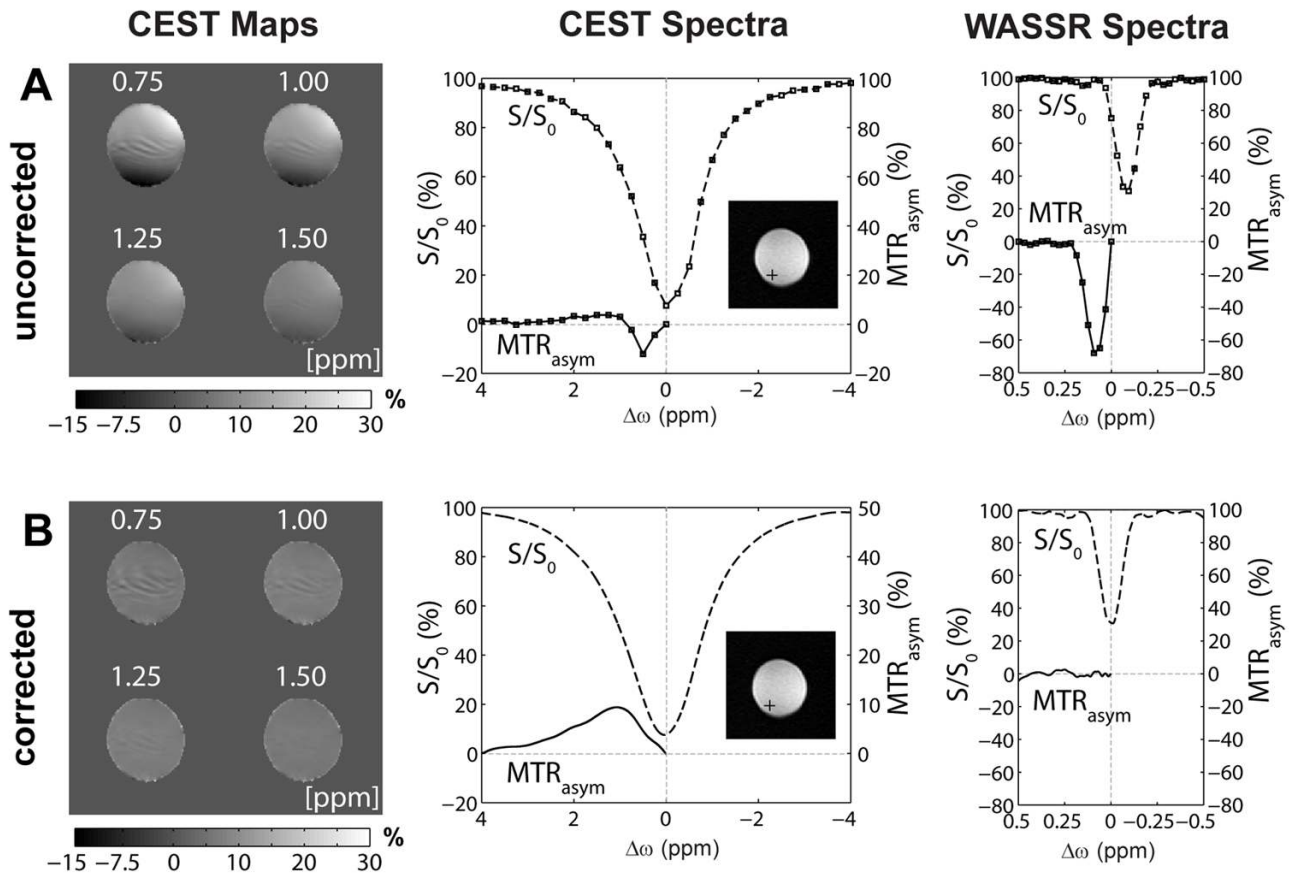dotted and dash-dotted lines show ± standard deviation.

Figure 4. CEST maps, single voxel-based Z-spectra and *MTR_asym* plots from CEST and WASSR obtained for the 200 mM glycogen phantom before (A) and after (B) WASSR correction
Z-spectra and *MTR_asym* plots are dashed and bold, respectively. The CEST maps are shown at offsets of 0.75, 1, 1.25 and 1.5 ppm (glycogen range). (A) glycoCEST maps before correction show a large spatial intensity fluctuation over the phantom. However, erroneous centering is not obvious in the Z-spectra (dashed line) due to the broad and flat curve bottom while the presence of glycogen is unclear in the *MTR_asym* plots (bold line). The WASSR Z-spectra (dashed line) acquired in the same voxel in the phantom clearly shows a shifted water center (bold line). (B) The WASSR-corrected CEST maps show remarkable improvement in image homogeneity. The CEST spectra show maximum signal up to around 11% for the phantom in the range of about 0.75–1.25 ppm frequency offset from water, which corresponds to the expected glycogen OH proton frequency range. Note the negligible *MTR_asym* in the WASSR plot due to proper centering of water frequency.
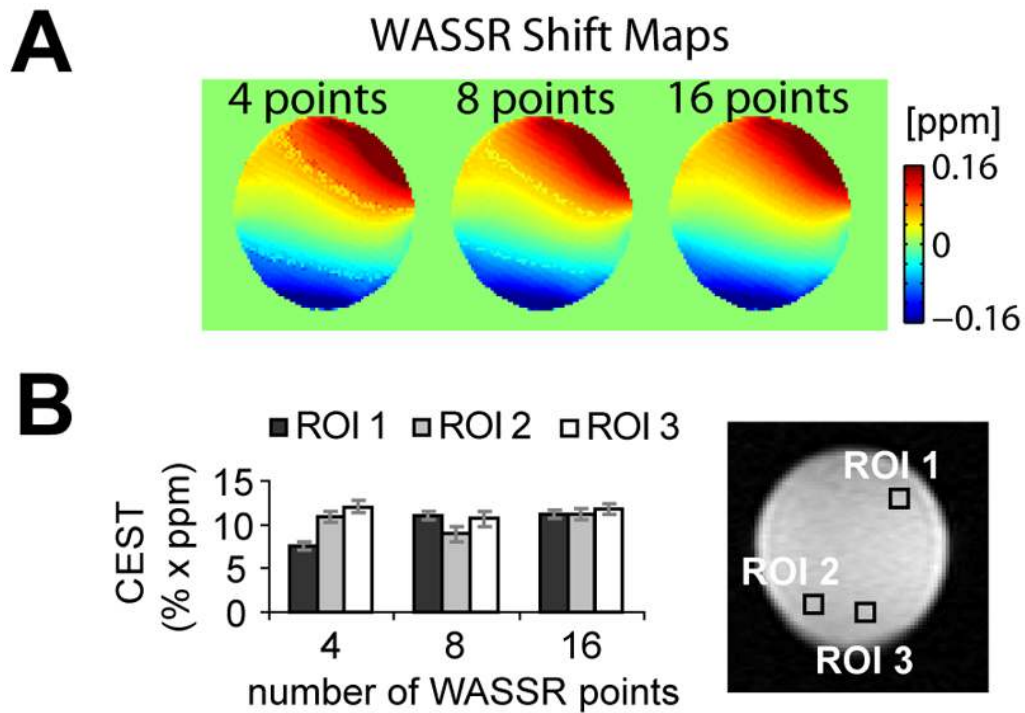
Figure 5. WASSR shift maps and quantification of glycoCEST MTR_{asym} as a function of number of WASSR points for the glycogen phantom
WASSR data initially acquired with thirty-three points within 1 ppm (± 0.5 ppm) were rearranged with three sets of WASSR data as following: four points within 0.375 ppm, eight points within 0.5 ppm and sixteen points within 0.5 ppm. (A) WASSR shift maps show that more detailed information becomes visible when using more points, in line with the simulations in Fig. 3. (B) Three different regions of 12 ± 2.7 voxels were defined as shown in a scout phantom image (right). Insufficient WASSR sampling results in inhomogeneous and erroneous CEST MTR_{asym} signal in these regions, and a minimum of 16 points over 0.5 ppm was needed to properly quantify the integral.
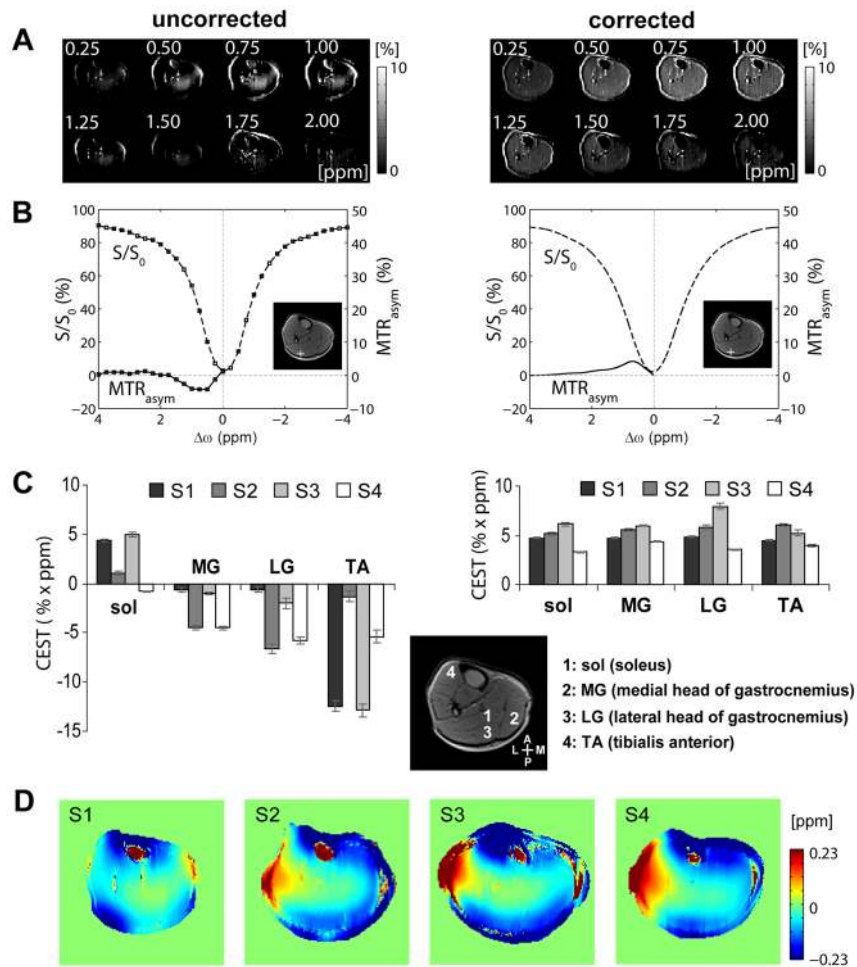
Figure 6. glycoCEST maps in human calf muscle before and after WASSR correction
(A) CEST maps before correction (left) show a large spatial intensity fluctuation over the entire calf muscle, while the WASSR-corrected maps (right) show remarkable improvement in image homogeneity. (B) The glycogen CEST effect can not be identified without B_0 correction, as shown in the MTR_{asym} plot (left), while the corrected MTR_{asym} plot (right) clearly displays the glycogen CEST effect (0–2 ppm frequency range), known to correspond to the glycogen OH protons. (C) Quantification of MTR_{asym} signal (integral over 0–2 ppm range) for four different muscle regions of 35 ± 0.4 (mean $\pm$ STD) voxels. All subjects show consistent CEST signal with WASSR-correction (right), while uncorrected CEST plots show erroneous and negative CEST signal (left). (D) The corresponding WASSR shift maps for each subject. Abbreviations: sol, soleus; MG, medial head of gastrocnemius; LG, lateral head of gastrocnemius; TA, tibialis anterior; A, anterior; P, posterior; L, lateral; M, medial.

Table 1

WASSR and CEST imaging parameters utilized in this study.

		duration (ms)	power (μT)	offset range (ppm)	number of offsets	FOV (mm^2)	NEX	time (min:sec)
phantom	**WASSR**	50	0.10	−0.5 to 0.5	33	100 × 100	1	3:33
	CEST	500	1.50	−4 to 4	33	100 × 100	1	3:33
Calf muscle	**WASSR**	100	0.25	−1 to 1	33	160 × 160	1	3:33
	CEST	500	0.75	−4 to 4	33	160 × 160	1	3:33

To determine S0, two additional data points were acquired; one with saturation pulse at 15.63 ppm and one without saturation

Parameters in table are not optimized in terms of timing; total scan time can be reduced by decreasing the acquisition matrix size and number of offset points (see text).

The offset is chemical shift difference with respect to water frequency.

Table 2

Dependence of WASSR-corrected glycoCEST MTR_{asym}[†] in the 200 mM glycogen phantom on the number of WASSR points.

	4 points	8 points	16 point
ROI 1	7.5	11.0	11.2
ROI 2	10.9	8.9	11.2
ROI 3	12.0	10.7	12.2
Mean	**10.1**	**10.2**	**11.5**
STD	**2.3**	**1.1**	**0.6**

[†] from the integral over the range of 0–2 ppm in the Z-spectrum (units ppm x %).

The values in the table are also plotted as bar graphs in Panel B of Fig. 5.

Table 3

WASSR-corrected glycoCEST MTR_{asym}[†] for in vivo calf muscle

	sol	MG	LG	TA
S1	4.8	4.7	4.8	4.5
S2	5.1	5.6	5.8	6.0
S3	6.1	6.0	7.9	5.3
S4	3.3	4.4	3.6	3.9
Mean	**4.8**	**5.2**	**5.5**	**4.9**
STD	**1.2**	**0.7**	**1.8**	**0.9**

[†]from the integral over the range of 0–2 ppm in the Z-spectrum (units ppm x %).

The values in the table are also plotted as bar graphs in Panel C of Fig. 6 on the right.

Abbreviations: sol, soleus; MG, medial head of gastrocnemius; LG, lateral head of gastrocnemius; TA, tibialis anterior.